Volume 7
Number 9
12 May 2026
Pages 4395–4930

Materials Advances

rsc.li/materials-advances

ISSN 2633-5409

ROYAL SOCIETY OF CHEMISTRY

PAPER

Ming Zhao, Shiqi Peng *et al.*
DTCC–RGDV: a nano-scaled conjugate capable of targeting arterial thrombi and releasing anti-thrombotic pharmacophore DTCC

Materials Advances

ROYAL SOCIETY OF CHEMISTRY

PAPER

View Article Online
View Journal | View Issue

Cite this: *Mater. Adv.*, 2026, 7, 4497

DTCC–RGDV: a nano-scaled conjugate capable of targeting arterial thrombi and releasing anti-thrombotic pharmacophore DTCC

Xiaoyi Zhang,[ab] Yifan Yang,[ab] Dongxu Wu,[ab] Yaonan Wang,[ab] Shurui Zhao,[ab] Jianhui Wu,[ab] Ming Zhao*[abc] and Shiqi Peng *[ab]

Received 18th March 2026,
Accepted 3rd April 2026

DOI: 10.1039/d6ma00386a

rsc.li/materials-advances

By docking into the active pockets of P-selectin and GPIIb/IIIa, virtual screening identified (3*S*)-1-[(5,5-dimethyl-3,4-dioxan-1-yl)-1,2,3,4-tetrahydro-β-carboline-3-carboxylic acid (DTCC) as a potential lead compound. The *in vivo* evaluation of DTCC was then performed in a rat thread model, and the arterial thrombus weight of the rats orally treated with 1 μmol kg^{-1} DTCC was significantly lower than that of the rats orally treated with NS and 20 μmol kg^{-1} RGDV (Arg-Gly-Asp-Val). Therefore, DTCC was coupled with RGDV, and a series of research studies on DTCC–RGDV were conducted. It was found that DTCC–RGDV was able to form a trimer, thereby forming nanoparticles with a diameter suitable for safe transport *via* blood circulation to bind to the surface of the platelets, simultaneously decreasing plasma P-selectin and GPIIb/IIIa levels to target the arterial thrombus and releasing the anti-arterial thrombus-active DTCC. Owing to the above-mentioned benefits, DTCC–RGDV did not cause kidney and liver injury in the treated rats.

Introduction

Coronary artery disease, acute ischemic stroke, and peripheral artery disease are the leading causes of death globally with high morbidity and mortality.[1,2] Arterial thrombosis is a critical factor underlying age-related major adverse cardiovascular events.[3] For patients with hypercoagulable states, arterial thrombosis is observed only in specific cases.[4] Cardiac tumors are usually related to the formation of atrial tumor thrombi.[5] The formation of atrial thrombi is mainly due to sustained platelet activation.[6] $FeCl_3$ treatment could be used to induce carotid arterial thrombosis in mice.[7] Downstream thromboembolism and arterial rupture are the acute and the late complications of basilar artery thrombosis.[8] Abdominal aortic tumor-thrombi may induce acute arterial occlusion.[9] Elevated plasma levels of factor VIII in erosive smooth muscle cell-rich neointima enhance arterial thrombus formation.[10] Accelerated arterial thrombosis contributes to Hutchinson–Gilford progeria syndrome.[11] Treating persistent left atrial appendage thrombosis remains a clinical challenge.[12]

To develop therapeutic agents for inhibiting arterial thrombosis, a series of efforts were made.[13–20] As one of the efforts, in a previous research study, we have disclosed that P-selectin and GPIIb/IIIa were simultaneously inhibited by (1*R*,3*S*)-1-methyl-1,2,3,4-tetrahydro-β-carboline-3-carboxylic acid.[21] Encouraged by this, in the present study, P-selectin and GPIIb/IIIa were used as the molecular target for virtual screening to develop a novel (3*S*)-1,2,3,4-tetrahydro-β-carboline-3-carboclic acid. To achieve this purpose, nine (3*S*)-1-substituted-1,2,3,4-tetrahydro-β-carboline-3-carboclic acids (STCCs) were designed and docked into the active pocket of P-selectin (PDB: 1G1R) and GPIIb/IIIa (PDB: 3ZDZ) for virtual screening. The virtual screening indicated that DTCC had the lowest docking energy. In this case, this paper aims to advance related research at DTCC.

Experimental

General

The solvents used in this experiment were purchased from Sinopharm Chemical Reagent Co., Ltd and were distilled and dried before use. The reagents were purchased from J&K

[a] *Beijing Area Major Laboratory of Peptide and Small Molecular Drugs, Department of Medicinal Chemistry, School of Pharmaceutical Sciences, Capital Medical University, NO. 10, Youanmenwaixitoutiao, Fengtai District, Beijing 100069, China. E-mail: maouzhao@126.com, sqpeng@bjmu.edu.cn; Fax: +861083911535; Tel: +861083911533*

[b] *Engineering Research Center of Endogenous Prophylactic of Ministry of Education of China, Department of Medicinal Chemistry, School of Pharmaceutical Sciences, Capital Medical University, NO. 10, Youanmenwaixitoutiao, Fengtai District, Beijing 100069, China*

[c] *Beijing Laboratory of Biomedical Materials and Key Laboratory of Biomedical Materials of Natural Macromolecules, Department of Biomaterials, College of Materials Science and Engineering, Beijing University of Chemical Technology, Beijing 100026, China*

Scientific® or from Sigma. The reaction was carried out under nitrogen flow (1 bar). ^{1}H (300 MHz or 800 MHz) and ^{13}C (75 MHz or 200 MHz) NMR spectra were recorded using a Bruker AMX-300 (AVANCE II) instrument. DMSO-d_6 and tetramethylsilane were the solvent and the internal standard, respectively. Using a 9.4 T solariX Fourier transform ion cyclotron resonance mass spectrometer (Bruker Corp, Billerica, MA, USA), FT-ICR-MS spectra were recorded. Chromatography was performed using Sephadex-LH_{20}, Qingdao silica gel GF_{254}, or Qingdao silica gel H_{60}. HPLC purity was measured using a Waters HPLC system (Waters Gradient Module 2545 with UV/visible detector 2489, sample manager 2767, and Waters CSH C18 column: 3.5 μm, 4.6 × 150 mm). The mobile phase of HPLC consisted of 50% methanol and 50% water plus 1/1000 formic acid, and the column temperature was 25 °C. AFM images were recorded using a Nanoscope 3D AFM or Multimode 8 instrument (Veeco Metrology, Santa Barbara, CA, USA) with the Nanoscope V531r1 software. The TEM and SEM images were acquired using S-4800 (Hitachi, Tokyo, Japan) and JSM-2100LV (JEOL, Tokyo, Japan), respectively. The chemical methods employed in this work were based on those previously published by our research group.[22,23]

Animal

Male ICR rats (230–270 g) were purchased from the Laboratory Animal Center of Capital Medical University. All evaluations were based on the protocol. The protocol was reviewed and approved by the Ethics Committee of Capital Medical University. The committee assured that the animal welfare was maintained in accordance with the requirements of the Animal Welfare Act and NIH Guide for Care and Use of Laboratory Animals.

Statistical analyses

Statistical analyses of all biological data were performed using one-way ANOVA. All analyses were performed using the SPSS 19.0 program, and a *P*-value less than 0.05 was considered statistically significant.

Synthesis

Preparation of benzyl (3*S*)-1,1-bis(hydroxymethyl)-1,2,3,4-tetrahydro-β-carboline-3-carboxylate (1). At 0 °C, into a solution of 1.0 g (3.6 mmol) of L-Trp-OBzl and 10 mL of dichloromethane, 0.5 mL of trifluoroacetic acid was added dropwise. At 0 °C, the reaction mixture was stirred, and 0.39 g (4.3 mmol) of 1,3-dihydroxyacetone was added. At room temperature, the reaction mixture was stirred for 7 h, and TLC (CH_2Cl_2/CH_3OH, 30/1) indicated the complete disappearance of L-Trp-OBzl. Then, the reaction mixture was neutralized with 30 mL of aqueous $NaHCO_3$ (10%). The CH_2Cl_2 phase was successively washed with aqueous $NaHCO_3$ (10%, 30 mL × 2) and aqueous NaCl (25%, 30 mL × 2). The CH_2Cl_2 phase was separated, dried with anhydrous Na_2SO_4 for 12 h, and then filtered. The filtrate was evaporated in a vacuum to give 1.01 g (81%) of benzyl (3*S*)-1,1-bis(hydroxymethyl)-1,2,3,4-tetrahydro-β-carboline-3-carboxylate (**1**) as a yellow powder. ESI(+)-FT-ICR-MS (*m*/*z*): 367.16543 $[M + H]^+$, (theoretical value: 367.16578). ^{1}H NMR (DMSO-d_6, 300 MHz): δ/ppm = 2.52 (m, 2H), 3.00 (dd, J_1 = 6.5 Hz, J_2 = 5.3 Hz, 1H), 3.56 (m, 3H), 3.77 (m, 1H), 4.03 (m, 1H), 4.81 (s, 2H), 5.23 (m, 2H), 6.98 (dt, J_1 = 6.7 Hz, J_2 = 5.6 Hz, 2H), 7.40 (m, 7H), 10.57 (s, 1H).

Preparation of benzyl (3*S*)-1-[(5,5-dimethyl-3,4-dioxan-1-yl)-1,2,3,4-tetrahydro-β-carboline-3-carboxylate (2). At 0 °C, 0.8 g (2.2 mmol) of **1** was dissolved in 16 mL of acetone, and then, 400 μL of concentrated H_2SO_4 and 316 mg (2.6 mmol) of anhydrous $MgSO_4$ were added. At room temperature, the reaction mixture was stirred for 8 hours, TLC (petroleum/ethyl acetate, 4/1) indicated the complete disappearance of **1**, and the reaction mixture was filtered, after which the filtrate was treated with aqueous $NaHCO_3$ (10%) and the reaction mixture was adjusted to pH 8 and evaporated in vacuum. The residue was washed with ethyl acetate (20 mL × 3) and aqueous NaCl (25%, 30 mL × 3) successively. The ethyl acetate phase was separated, dried with anhydrous Na_2SO_4 for 12 hours, and then filtered. The filtrate was evaporated in a vacuum, and the residue was purified on a silica gel column (petroleum/ethyl acetate, 4/1). Then, 0.33 g (37%) of benzyl (3*S*)-1-[(5,5-dimethyl-3,4-dioxan-1-yl)-1,2,3,4-tetrahydro-β-carboline-3-carboxylate (**2**) was obtained as a colorless powder. ESI(+)-FT-ICR-MS (*m*/*z*): 407.19691 $[M + H]^+$ (theoretical value: 407.19703); ^{1}H NMR (DMSO-d_6, 300 MHz): δ/ppm = 1.38 (s, 3H), 1.62 (s, 3H), 2.72 (m, 1H), 3.04 (m, 1H), 3.85 (d, J = 6.2 Hz, 1H), 3.52 (d, J = 6.2 Hz, 1H), 3.99 (m, 2H), 4.46 (d, J = 5.2 Hz, 1H), 5.26 (s, 2H), 7.03 (dt, J_1 = 5.1 Hz, J_2 = 7.5 Hz, 2H), 7.40 (m, 7H), 11.05 (s, 1H). ^{13}C NMR (DMSO-d_6, 75 MHz): δ/ppm = 19.3, 25.6, 29.1, 51.8, 63.8, 66.5, 68.8, 98.1, 108.7, 111.7, 118.3, 119.1, 121.7, 126.7, 128.3, 128.6, 129.0, 133.2, 136.5, 136.6, 172.9.

Preparation of (3*S*)-1-[(5,5-dimethyl-3,4-dioxan-1-yl)-1,2,3,4-tetrahydro-β-carboline-3-carboxylic acid (3, DTCC). At room temperature, a suspension of 5 mL of methanol, 285 mg (0.7 mmol) of benzyl (3*S*)-1-[(5,5-dimethyl-3,4-dioxan-1-yl)-1,2,3,4-tetrahydro-β-carboline-3-carboxylate (**2**), and 30 mg of Pd/C was agitated for 12 hours with hydrogen gas, and TLC (petroleum/ethyl acetate, 4/1) indicated the complete disappearance of **2**. The reaction mixture was filtered, the filtrate was evaporated in a vacuum, and the residue was washed with ether (40 mL × 3). Then, 201 mg (91%) of DTCC was obtained as a colorless powder. ESI(-)-FT-ICR-MS (*m*/*z*): 315.13382 $[M–H]^-$ (theoretical value: 315.13448). HPLC purity: 99.4%. ^{1}H NMR (DMSO-d_6, 300 MHz): δ/ppm = 1.40 (s, 3H), 1.63 (s, 3H), 2.67 (m, 1H), 3.02 (dd, J_1 = 7.0 Hz, J_2 = 5.3 Hz, 1H), 3.56 (d, J = 6.2 Hz, 1H), 3.83 (m, 2H), 4.03 (d, J = 6.2 Hz, 1H), 4.48 (d, J = 6.2 Hz, 1H), 7.04 (dt, J_1 = 5.1 Hz, J_2 = 7.5 Hz, 2H), 7.40 (dt, J_1 = 6.8 Hz, J_2 = 6.2 Hz, 2H), 11.07 (s, 1H). ^{13}C NMR (DMSO-d_6, 75 MHz): δ/ppm = 19.5, 25.6, 29.1, 51.8, 52.0, 63.8, 68.7, 98.2, 109.2, 111.7, 118.3, 119.1, 121.7, 126.7, 133.0, 136.7, 174.3.

Preparation of Boc-Arg(NO_2)-Gly-OBzl. At 0 °C, a solution of 751 mg (3.6 mmol) of DCC was added dropwise to a suspension of 960 mg (3.0 mmol) of Boc-Arg(NO_2), 30 mL of THF, and 450 mg (3.3 mmol) of HOBt and then stirred for 30 minutes to provide solution A. At 0 °C, a solution of 1.11 g (3.3 mmol) of Tos·Gly-OBzl in 10 mL of anhydrous THF was prepared and the pH was adjusted to 8 with NMM to provide solution B. At room temperature, solution A and solution B were mixed, stirred for

12 hours, and TLC (CH_2Cl_2/CH_3OH, 20/1) indicated the complete disappearance of Boc-Arg(NO_2) and Gly-OBzl. To the reaction mixture, 10 mL of ethyl acetate was added, and then, it was filtered to remove insoluble matter. The filtrate was successively washed with a saturated solution of sodium bicarbonate in water (30 mL × 3), a saturated solution of sodium chloride (30 mL × 3), 5% solution of potassium bisulfate in water (30 mL × 3), a saturated solution of sodium bicarbonate in water (30 mL × 3), and a saturated solution of sodium chloride in water (30 mL × 3). The solution was dried with anhydrous sodium sulfate for 12 hours and then filtered. The filtrate was evaporated in a vacuum, and a yellowish syrup was obtained. To the yellowish syrup, 30 mL of dichloromethane was added to precipitate 1.23 g (88%) of Boc-Arg(NO_2)-Gly-OBzl, which was obtained as a colorless powder. ESI(+)-FT-ICR-MS (*m*/*z*): 467.22552 $[M + H]^+$(theoretical value: 467.22542); ^{1}H-NMR (300 MHz, DMSO-d_6): δ/ppm = 8.48 (s, 1H), 8.26 (t, J = 5.4 Hz, 1H), 7.35 (m, 5H), 6.87 (d, J = 8.2 Hz, 1H), 5.12 (s, 2H), 3.89 (m, 3H), 3.11 (m, 2H), 2.45 (m, 2H), 1.50 (m, 4H), 1.38 (s, 3H), 1.37 (s, 3H), 1.36 (s, 3H).

Preparation of Boc-Arg(NO_2)-Gly. At 0 °C, 935 mg (2.0 mmol) of Boc-Arg(NO_2)-Gly-OBzl was dissolved in 10 mL of methanol, the solution was treated with a solution of sodium hydroxide in water (2N) for 4 hours, and TLC (petroleum/ethyl acetate, 3/1) indicated the complete disappearance of Boc-Arg(NO_2)-Gly-OBzl. The reaction mixture was quickly acidified with hydrochloric acid, and the solution was evaporated in a vacuum. The residue was dissolved in 60 mL of ethyl acetate, and the solution was washed with the saturated solution of sodium chloride in water (30 mL × 3). The solution was dried with anhydrous Na_2SO_4 for 12 hours and then filtered. The filtrate was evaporated in a vacuum, and 635 mg (84%) of Boc-Arg(NO_2)-Gly was obtained as a colorless powder. ESI(+)-FT-ICR-MS (*m*/*z*): 377.17832 $[M + H]^+$(theoretical value: 377.17847).

Preparation of Boc-Asp(OBzl)-Val-OBzl. Using 970 mg (3.0 mmol) of Boc-Asp(OBzl) and 805 mg (3.3 mmol) of Val-OBzl, the procedure for preparing Boc-Arg(NO_2)-Gly-OBzl yielded 1.33 g (87%) of Boc-Asp(OBzl)-Val-OBzl as colorless powders. ESI(+)-FT-ICR-MS (*m*/*z*): 513.26112 $[M + H]^+$(theoretical value: 513.26008); ^{1}H NMR (DMSO-d_6, 300 MHz): δ/ppm = 0.85 (d, J = 6.0 Hz, 3H), 0.86 (d, J = 6.0 Hz, 3H), 1.37 (s, 3H), 1.38 (s, 3H), 1.39 (s, 3H), 2.05 (m, 1H), 2.65 (m, 2H), 4.24 (t, J = 6.2 Hz, 1H), 4.45 (m, 1H), 5.13 (m, 4H),7.2 9(m, 11H), 8.01 (d, J = 5.9 Hz, 1H).

Preparation of Asp(OBzl)-Val-OBzl. At 0 °C, 1.02 g (2.0 mmol) of Boc-Arg(OBzl)-Val-OBzl was treated with 10 mL of a solution of hydrogen chloride in ethyl acetate for 4 hours, and TLC (petroleum/ethyl acetate, 3/1) indicated the complete disappearance of Boc-Arg(OBzl)-Val-OBzl. The reaction mixture was evaporated in a vacuum, the residue was dissolved in 5 mL of anhydrous ethyl acetate, and the solution was evaporated in a vacuum. This procedure was repeated three times to provide 0.80 g (90%) of Asp(OBzl)-Val-OBzl as a colorless powder. ESI(+)-FT-ICR-MS (*m*/*z*): 413.20722 $[M + H]^+$ (theoretical value: 413.20765).

Preparation of Boc-Arg(NO_2)-Gly-Asp(OBzl)-Val-OBzl. Using 565 mg (1.5 mmol) of Boc-Arg(NO_2)-Gly and 718 mg (1.6 mmol) of Asp(OBzl)-Val-OBzl, the procedure for preparing Boc-Arg(NO_2)-Gly-Asp(OBzl)-Val-OBzl yielded 1.01 g (88%) of the product as colorless powders. ESI(+)-FT-ICR-MS (*m*/*z*): 777.36725 $[M + H]^+$ (theoretical value: 777.36773); ^{1}H NMR (DMSO-d_6, 300 MHz): δ/ppm = 0.85 (d, J = 6.1 Hz, 6H), 1.37 (s, 3H), 1.38 (s, 3H), 1.39 (s, 3H), 1.58 (m, 4H), 2.07 (m, 1H), 2.57 (m, 1H), 2.76 (m, 1H), 3.12 (m, 2H), 3.71 (m, 2H), 3.94 (m, 1H), 4.18 (t, J = 6.1 Hz, 1H), 4.77 (m, 1H), 5.09 (m, 4H), 6.97 (d, J = 6.2 Hz, 1H), 7.35 (m, 10H), 8.07 (s, 1H), 8.15 (d, J = 6.1 Hz, 1H), 8.21 (d, J = 6.9 Hz, 1H), 8.49 (s, 1H).

Preparation of Arg(NO_2)-Gly-Asp(OBzl)-Val-OBzl. By use of the procedure of preparing Arg(OBzl)-Val-OBzl from 470 mg (0.7 mmol) of Boc-Arg(NO_2)-Gly-Asp(OBzl)-Val-OBzl, 435 mg (88%) of Arg(NO_2)-Gly-Asp(OBzl)-Val-OBzl was obtained as a colorless powder. ESI(+)-FT-ICR-MS (*m*/*z*): 671.36544 $[M + H]^+$ (theoretical value: 671.36530).

Preparation of (3*S*)-1-[(5,5-dimethyl-3,4-dioxan-1-yl)-1,2,3,4-tetrahydro-β-carboline-3-carboxyl-Arg(NO_2)-Gly-Asp(OBzl)-Val-OBzl (4). Following the procedure for preparing Boc-Arg(NO_2)-Gly-OBzl, 190 mg (0.6 mmol) of DTCC and 430 mg (0.61 mmol) of Arg(NO_2)-Gly-Asp(OBzl)-Val-OBzl were reacted to yield 520 mg (90%) of compound **4** as colorless powders. ESI(+)-FT-ICR-MS (*m*/*z*): 969.44697 $[M + H]^+$ (theoretical value: 969.44704); ^{1}H NMR (DMSO-d_6, 300 MHz): δ/ppm = 0.85 (d, J = 6.1 Hz, 6H), 1.39 (s, 3H), 1.62 (m, 7H), 2.07 (m, 1H), 2.27 (s, 1H), 2.62 (m, 2H), 2.67 (m, 1H), 3.03 (m, 2H), 3.16 (m, 2H), 3.68 (m, 5H), 3.99 (d, J = 6.2 Hz, 1H), 4.19 (t, J = 6.2 Hz, 1H), 4.38 (m, 2H), 4.78 (m, 1H), 5.08 (m, 4H), 6.97 (t, J = 6.1 Hz, 1H), 7.07 (t, J = 6.1 Hz, 1H), 7.35 (m, 12H), 8.02 (d, J = 6.9 Hz, 1H), 8.17 (d, J = 6.1 Hz, 1H), 8.31 (m, 2H), 8.54 (s,1H), 10.92 (s, 1H); ^{13}C NMR (DMSO-d_6, 75 MHz): δ/ppm = 18.6, 19.4, 20.3, 26.3, 28.2, 29.6, 30.3, 36.6, 42.4, 49.6, 51.6, 52.7, 53.0, 55.5, 58.1, 64.7, 66.1, 66.4, 66.5, 68.5, 98.1, 109.0, 111.7, 118.1, 119.1, 121.6, 126.7, 128.3, 128.4, 128.5, 128.6, 128.8, 128.9, 133.8, 136.3, 136.4, 136.5, 159.7, 169.2, 170.3, 171.1, 171.5, 172.2, 173.4.

Preparation of (3*S*)-1-[(5,5-dimethyl-3,4-dioxan-1-yl)-1,2,3,4-tetrahydro-β-carboline-3-carboxyl-Arg-Gly-Asp-Val (5, DTCC–RGDV). By use of the procedure of preparing DTCC from 485 mg (0.5 mmol) of (3*S*)-1-[(5,5-dimethyl-3,4-dioxan-1-yl)-1,2,3,4-tetrahydro-β-carboline-3-carboxyl-Arg(NO_2)-Gly-Asp(OBzl)-Val-OBzl (**4**), 340 mg (92%) of DTCC–RGDV were obtained as a colorless powder. FT-ICR-MS (*m*/*z*): 744.36811 $[M + H]^+$ (theoretical value, 744.36806); ^{1}H NMR (DMSO-d_6, 800 MHz): δ/ppm = 0.91 (d, J = 6.1 Hz, 3H), 0.92 (d, J = 6.1 Hz, 3H), 1.40 (s, 3H), 1.41 (s, 3H), 1.52 (m, 2H), 1.78 (m, 2H), 1.90 (m, 1H), 1.91 (s, 1H), 2.66 (s, 1H), 2.66 (d, J = 5.4 Hz, 1H), 2.73 (d, J = 6.6 Hz, 1H), 2.92 (d, J = 5.4 Hz, 1H), 2.93 (d, J = 6.6 Hz, 1H), 3.33 (m, 2H), 3.34 (m, 2H), 3.97 (s, 1H), 3.98 (s, 1H), 3.99 (t, J = 5.4 Hz, 1H), 4.11 (s, 2H), 4.24 (s, 1H), 4.25 (s, 1H), 4.26 (d, J = 6.3 Hz, 1H), 4.84 (t, J = 6.6 Hz, 1H), 6.65 (s, 2H), 6.94 (d, J = 8.1 Hz, 1H), 6.96 (t, J = 8.1 Hz, 1H), 7.21 (d, J = 8.0 Hz, 1H), 7.36 (d, J = 8.0 Hz, 1H), 7.85 (s, 1H), 8.32 (s, 1H), 8.33 (s, 1H), 8.35 (s, 1H), 9.05 (s, 1H), 11.64 (s,1H), 12.39 (s, 1H); ^{13}C NMR (DMSO-d_6, 200 MHz): δ/ppm = 18.91, 18.92, 24.33, 25.38, 25.37, 26.32, 26.33, 31.22, 37.18, 42.19, 43.51, 53.42, 56.76, 61.75, 66.25, 67.19, 76.13, 76.15,

108.18, 113.98, 111.17, 118.25, 119.71, 121.59, 126.77, 135.59, 136.25, 157.93, 170.38, 170.98, 172.79, 173.22, 174.81, 175.16; HPLC purity: 97.6%.

Nano-characterization

TEM image and nano-property of DTCC–RGDV

Transmission electron microscopy (TEM, JSM-2100LV, JEOL, Tokyo, Japan) was utilized to show the shape and size of the nanoparticles of DTCC–RGDV. Onto a formvar-coated copper grid, the solution of DTCC–RGDV in ultrapure water (1 μM, 0.1 μM, and 0.01 μM) was dripped, air-dried, and heated at 37 °C for 14 days. The grids were observed under a microscope. *Via* more than 100 species of randomly selected regions, the nanoparticles of DTCC–RGDV were counted. An imaging plate (Gatan Bioscan Camera Model 1792, Pleasanton, CA, USA) was used to record 6000–400 000× digitally enlarged TEM images of DTCC–RGDV, and the energy was 20 eV. At an 80 kV electron beam of accelerating voltage, each sample was imaged with triplicate grids.

SEM image and nano-property of DTCC–RGDV

To study the shape and size of lyophilized powders, scanning electron microscopy (SEM, S-4800, Hitachi, Tokyo, Japan) was performed at 50 kV. The lyophilized powders from the solution of DTCC–RGDV in ultrapure water (1 μM, 0.1 μM, and 0.01 μM) were attached to a copper plate with double-sided tape (Euromedex, Strasbourg, France). By using a Joel JFC-1600 Auto Fine Coater (JEOL, Japan), the samples were coated with 20 nm of gold-palladium at 15 kV, 30 mA, and 200 mTorr (argon) for 60 s. On the SEM alloy of a randomly selected region, more than 100 species were examined to identify the features and size of the lyophilized powders of DTCC–RGDV. Triplicate grids were prepared for testing each sample. An imaging plate (Gatan Bioscan Camera Model 1792) with 20 eV-energy windows was utilized to record 100–10 000× digitally enlarged SEM images.

AFM image and nano-property of DTCC–RGDV

At 22 °C, with contact mode, the images of atomic force microscopy (AFM) were recorded for the solution of DTCC–RGDV in rat plasma (1 μM, 0.1 μM, and 0.01 μM), and a nanoscope 3D AFM (Veeco Metrology, Santa Barbara, CA, USA) was used.

Particle size and zeta potential of DTCC–RGDV

To show the nano-property of the solution of DTCC–RGDV in ultrapure water (1 μM, 0.1 μM, and 0.01 μM), the Tyndall effect and particle size were tested using a particle size analyzer (Nano-ZS90; Malvern Instruments Ltd, Malvern, UK). To show the stability of the nano-property of the solution of DTCC–RGDV in ultrapure water (1 μM), the zeta potential was tested using a zeta potential plus analyzer (Brookhaven Instruments Corp, Holtsville, NY, USA). To show the effect of time on the stability of the nano-property, the solution of DTCC–RGDV in ultrapure water (1 μM) was tested at 25 °C for 7 days. Each test was repeated three times.

In vitro interaction assay

UV-based *in vitro* interaction between DTCC and P-selectin

To study the *in vitro* interaction between DTCC and P-selectin, the UV spectra of DTCC in ultrapure water (1 nM) with P-selectin (8 pg mL^{-1}, 16 pg mL^{-1}, and 32 pg mL^{-1}, ELISA kit of rat P-selectin, Shanghai MLBIO Biotechnology Co. Ltd, China) were recorded (250–500 nm of wavelength, UV-2600, Shimadzu, Japan).

UV-based *in vitro* interaction between DTCC and GPIIb/IIIa

To study the *in vitro* interaction between DTCC and GPIIb/IIIa, the UV spectra of DTCC in ultrapure water (1 nM) with GPIIb/IIIa (200 U mL^{-1}, 400 U mL^{-1}, and 800 U mL^{-1}, ELISA kit of rat GPIIb/IIIa, Shanghai MLBIO Biotechnology Co. Ltd, China) were recorded (250–500 nm of wavelength, UV-2600, Shimadzu, Japan)

CD-based *in vitro* interaction between DTCC and P-selectin

To study the *in vitro* interaction between DTCC (in ultrapure water of pH 6.7, 0.5 nM, 1 nM, and 2 nM) and P-selectin (32 pg mL^{-1}, ELISA kit of rat P-selectin, Shanghai MLBIO Biotechnology Co. Ltd, China), the CD (circular dichroism) spectra were recorded (200–400 nm of wavelength, J-810, Jasco, Japan).

CD-based *in vitro* interaction between DTCC and GPIIb/IIIa

To study the *in vitro* interaction between DTCC (in ultrapure water of pH 6.7, 0.5 nM, 1 nM, and 2 nM) and GPIIb/IIIa (800 U mL^{-1}, ELISA kit of rat GPIIb/IIIa, Shanghai MLBIO Biotechnology Co. Ltd, China), the CD spectra were recorded (200–400 nm of wavelength, J-810, Jasco, Japan).

AFM-imaged *in vitro* action of DTCC–RGDV in rat erythrocytes

To visualize the action of DTCC–RGDV in erythrocytes, the arterial blood of a rat was sampled and treated using a kit by following the manufacturer's specifications (RBC2012RATK, TBD Science, Tianjin, China). The sample diluents (from the kit) were added into the blood (volume ratio: 1/1) and evenly mixed. The diluted blood was carefully added into the separation liquid (from the kit) (volume ratio: 1/1), evenly mixed, and centrifuged at 850 g for 30 minutes to promote the sample to form a plasma layer, leukocyte layer, separation liquid layer, and erythrocyte layer. The erythrocyte layer was sampled, mixed with 10 mL of washing solution, evenly mixed, and centrifuged at 250 g for 10 minutes. The erythrocytes were successively resuspended in 5 mL of cleaning solution (from the kit) for washing (5 mL × 2) and 1.5 mL of NS (normal saline). Then, 10 μL of aqueous DTCC–RGDV in ultrapure water was added into 300 μL of the suspension (final concentration: 1 μM) and incubated at 37 °C for 30 minutes. Then 700 μL of electron microscope fixative was added and fixed for 5 hours. The suspension was washed three times with ultrapure water and sampled to observe the effect of the trimer of DTCC–RGDV on AFM morphology of rat erythrocytes (Veeco Metrology, Santa Barbara, CA, USA).

AFM image and the action of DTCC–RGDV in rat leukocytes *in vitro*

To visualize the action of DTCC–RGDV in leukocytes, the arterial blood of a healthy rat was sampled and treated by following the specifications of the kit (RBC2012RATK, TBD Science, Tianjin, China). The sample diluents (from the kit) were added into the blood, (volume ratio: 1/1) and evenly mixed. The diluted blood was carefully added into the separation liquid (from the kit) (volume ratio: 1/1), evenly mixed, and centrifuged at 850 g for 30 minutes to allow the sample to form a plasma layer, leukocyte layer, separation liquid layer, and erythrocyte layer. The leukocyte layer was sampled, mixed with 10 mL of washing solution, evenly mixed, and centrifuged at 250 g for 10 minutes. The leukocytes were successively resuspended in 5 mL of cleaning solution (from the kit) for washing (5 mL × 2) and 1.5 mL of NS. After that, 10 μL of aqueous DTCC–RGDV in ultrapure water (final concentration: 1 μM) was added into 300 μL of the suspension and incubated at 37 °C for 30 minutes. Then 700 μL of electron microscope fixative was added, and the sample was fixed at 4 °C for 5 hours. The suspension was washed three times with ultrapure water and sampled to observe the effect of trimer on the AFM morphology of DTCC–RGDV in rat leukocytes (Veeco Metrology, Santa Barbara, CA, USA).

AFM image and the action of DTCC–RGDV on rat platelets *in vitro*

Arterial blood (5 mL) from a healthy rat was collected into a silanized centrifuge tube, inhibited by 10% sodium citrate, and centrifuged at 250 g for 10 minutes. The upper white turbid liquid was transferred into another silanized centrifuge tube, and NS was added (volume ratio: 1/2). The diluted solution was centrifuged at 250 g for 10 minutes, and this procedure was repeated twice to obtain platelets, which were suspended in 1.5 mL of NS and divided into five portions. The platelets in each portion were treated with 30 μL of NS or 30 μL aqueous DTCC–RGDV in ultrapure water (final concentration: 1 μM) and incubated at 37 °C for 10 minutes. Then, 10 μL of NS or 10 μL solution of arachidonic acid (AA) was added to the platelets and incubated at 37 °C for another 20 minutes. At 4 °C, 700 μL of electron microscope fixative was added to AA-treated platelets for 5-hour fixation. The fixated platelets were centrifuged to remove the fixation liquid, suspended in 800 μL of ultrapure water, and sampled on a silicon plate to observe the AFM image (Veeco Metrology, Santa Barbara, CA, USA).

Bioassays

In vivo arterial thrombus weight assay for DTCC–RGDV

The anti-arterial thrombosis activity was evaluated in a rat thread model, and the thrombus weight was used to represent the activity. In this assay, NS (3 mL kg^{-1}, negative control), the suspension of aspirin in NS (16.7 μmol kg^{-1} and 167 μmol kg^{-1}, positive control), the suspension of DTCC in NS (1.0 μmol kg^{-1}, parent compound control), the solution of RGDV in NS (20.0 μmol kg^{-1}, parent compound control) and the suspension of DTCC–RGDV in NS (0.1 μmol kg^{-1}) were orally given to male Sprague-Dawley rats (230–270 g, each 12 rats). Thirty minutes after administration, the rats were anaesthetized with sodium pentobarbital (80.0 mg kg^{-1}, i.p.) to separate the right carotid artery and left jugular vein. An exactly weighted thread (6 cm in length) was put unto a polyethylene tube, which was filled with a solution of heparin sodium in NS (50 IU mL^{-1}). Two ends of the polyethylene tube were inserted into the left jugular vein and right carotid artery, respectively. Heparin sodium, the anticoagulant, was injected, the blood of the rat was allowed to flow through the polyethylene tube for 15 minutes, and the thread was taken out of the tube to weigh, while the increased weight of the thread was calculated to represent the activity. Finally, the blood of the rats was collected for various ELISA assays.

In vivo P-selectin assay for DTCC–RGDV

The incubation temperature of this assay was 37 °C. The blood of the rats treated with NS (3 mL kg^{-1}, negative control) or the blood of the rats treated with the suspension of DTCC–RGDV in NS (0.1 μmol kg^{-1}) was collected and mixed with 3.8% sodium citrate (volume ratio: 9/1). At 3000 g, the blood was centrifuged for 15 minutes, and the top layer was obtained as platelet-poor plasma (PPP). In the well, 100 μL of PPP was treated with rat P-selectin (rat P-selectin ELISA kit, CSB-E07399r, Cusabio Biotech, USA) and incubated for 120 minutes. After removing the solvent, 100 μL of biotin labeling antibody from the kit was added into each well and incubated for 60 minutes. The solution in the well was discarded, and the residue was washed with the washing solution of the kit (200 μL × 3). To each well, 100 μL of horseradish peroxidase-labeled avidin of the kit was added, incubated for 60 minutes, and washed with the washing solution of the kit (200 μL × 5). For coloration, 90 μL of the substrate solution of the kit was added to each well and incubated in the dark for 20 minutes. To each well, 50 μL of the stop solution of the kit was added to stop the reaction. The OD value of the well was measured at 450 nm within 15 minutes. The level of P-selectin in the plasma of the treated rats was calculated by following the standard curve (from the ELISA kit standard samples).

In vivo GPIIb/IIIa assay for DTCC–RGDV

The incubation temperature of this assay was 37 °C. The blood of the rats treated with NS (3 mL kg^{-1}, negative control) or the blood of the rats treated with the suspension of DTCC–RGDV in NS (0.1 μmol kg^{-1}) was collected and mixed with 3.8% sodium citrate (volume ratio: 9/1). At 3000 g, the blood was centrifuged for 15 minutes, and the top layer was obtained as platelet-poor plasma (PPP). In the well, 100 μL of PPP was treated with rat GPIIb/IIIa (rat GPIIb/IIIa ELISA kit, CSB-E08776r, Cusabio Biotech, USA) for 120 minutes. After removing the solvent, 100 μL of biotin labeling antibody of the kit was added to each well and incubated for 60 minutes. The solution in the well was discarded, and the residue was washed with the washing solution of the kit (200 μL × 3). To each well, 100 μL of

horseradish peroxidase-labeled avidin of the kit was added, incubated for 60 minutes, and washed with the washing solution of the kit (200 μL × 5). For coloration, 90 μL of the substrate solution of the kit was added to each well and then incubated in the dark for 20 minutes. To each well, 50 μL of the stop solution of the kit was added to stop the reaction. The OD value of the well was measured at 450 nm within 15 minutes. The level of GPIIb/IIIa in the plasma of the treated rats was calculated by following the standard curve (from rat GPIIb/IIIa ELISA kit standard samples).

DTCC–RGDV releasing DTCC in the arterial thrombus

By using a liquid–liquid extraction, the extracts of the thrombus, blood, heart, liver, spleen, kidney, and brain of the rats treated with NS and the extracts of the thrombus, blood, heart, liver, spleen, kidney, and brain of the rats treated with DTCC–RGDV were prepared for FT-ICR-MS analysis. Thrombus, blood, heart, liver, spleen, kidney, and brain were homogenized after dilution with ultrapure water and then extracted with ethyl acetate. The samples received ultrasonic extraction for 30 minutes and centrifugal separation for 15 minutes (4000 g). The upper layer was separated and evaporated over N2 gas at 37 °C. The residue was dissolved in chromatographically pure methanol (200 μL of methanol per g of tissue) for analysis.

Results and discussion

The docking energies of STCCs are shown in Table 1. As seen, among the nine STCCs, DTCC had the lowest energy for both P-selectin (−70.52 kcal mol^{-1}) and GPIIb/IIIa (−73.96 kcal mol^{-1}).

To confirm the credibility of the docking investigation-based virtual screening, DTCC was prepared, the *in vitro* interactions of DTCC with P-selectin and GPIIb/IIIa were measured, and the *in vivo* anti-arterial thrombosis action of DTCC was evaluated.

Fig. 1A indicates that P-selectin concentration dependently decreased the intensity of UV absorption of DTCC. This meant that P-selectin concentration dependently acted on DTCC. Fig. 1B indicates that the DTCC concentration dependently decreased the signal strength of CD of P-selectin. This meant that the DTCC concentration acted on P-selectin. Fig. 1C indicates that the GPIIb/IIIa concentration dependently decreased the intensity of UV absorption of DTCC. This meant that the GPIIb/IIIa concentration dependently acted on DTCC. Fig. 1D indicates that the DTCC concentration dependently decreased the signal strength of CD of GPIIb/IIIa. This meant that the DTCC concentration dependently acted on GPIIb/IIIa.

Fig. 2A indicates that the arterial thrombus weight of the rats orally treated with 1 μmol kg^{-1} of DTCC was significantly lower than the arterial thrombus weight of the rats orally treated with NS (blank control, $P < 0.01$). Fig. 2B indicates that the arterial thrombus weight of the rats orally treated with 1 μmol kg^{-1} of DTCC was significantly lower than the arterial thrombus weight of the rats orally treated with 20 μmol kg^{-1} of RGDV (pharmacophore control of DTCC–RGDV, $P < 0.05$). These data meant that DTCC could be used as an excellent pharmacophore for further investigation. Besides, the oral dose of RGDV was 20 times higher than the oral dose of DTCC. From the view of the anti-arterial thrombosis of DTCC, the anti-arterial thrombotic action of RGDV was found to be negligible.

Table 1 Docking energy of nine STCCs

STCCs	P-selectin, kcal mol^{-1}	GPIIb/IIIa, kcal mol^{-1}
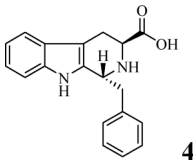 **4**	−39.31	−40.71
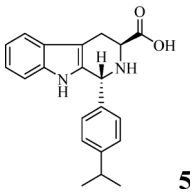 **5**	−24.77	−27.01
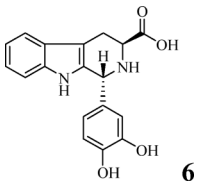 **6**	−26.56	−29.34
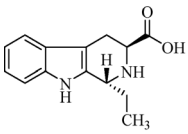 **7**	−27.71	−30.87
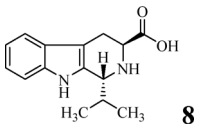 **8**	−28.99	−31.41
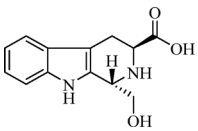	−30.22	−32.25
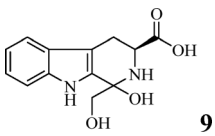 **9**	−40.85	−42.83
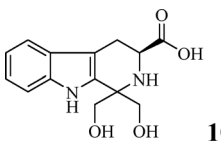 **10**	−41.65	−43.53
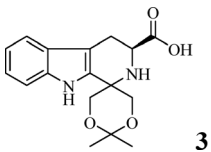 **3** DTCC	−70.52	−73.96

Synthetic route and HPLC purity of DTCC–RGDV

Scheme 1 shows the preparation of benzyl (3*S*)-1,1-bis-(hydroxymethyl)-1,2,3,4-tetra-hydro-β-3-carboxylate (**1**), benzyl

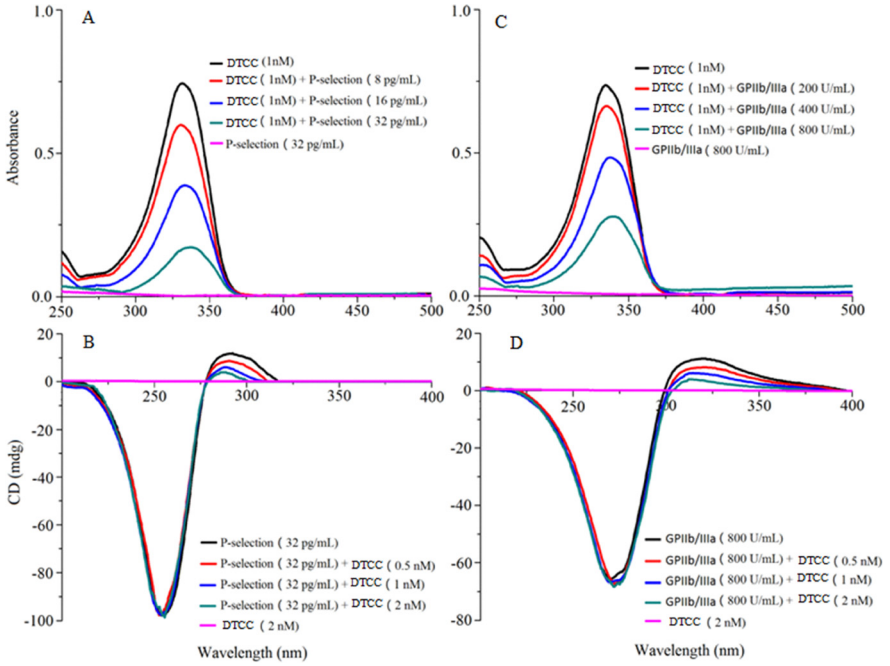

Fig. 1 *In vitro* interaction between DTCC with P-selectin and GPIIb/IIIa: (A) effect of P-selectin on the UV absorbance of DTCC; (B) effect of DTCC on the CD signal strength of P-selectin; (C) effect of GPIIb/IIIa on the UV absorbance of DTCC; and (D) effect of DTCC on the CD signal strength of GPIIb/IIIa.

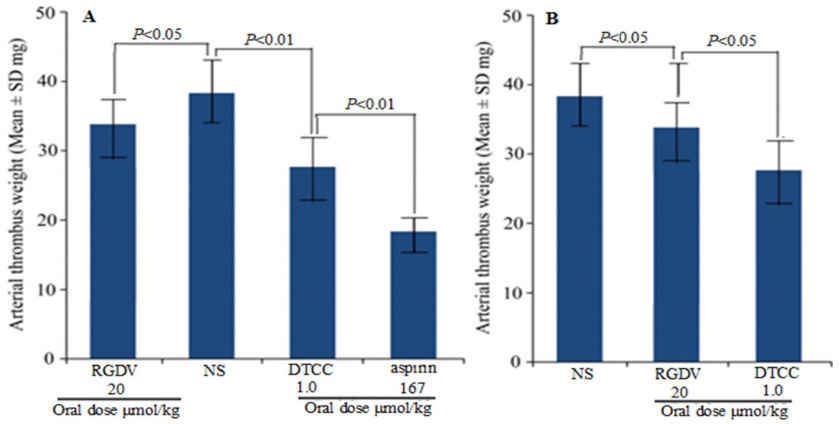

Fig. 2 *In vivo* anti-arterial thrombus activity of DTCC. (A) The arterial thrombus weight of the rats orally treated by 1 μmol kg^{-1} of DTCC was significantly lower than the arterial thrombus weight of the rats orally treated by NS (blank control, $P < 0.01$). (B) The arterial thrombus weight of the rats orally treated by 1 μmol kg^{-1} of DTCC was significantly lower than the arterial thrombus weight of the rats orally treated by 20 μmol kg^{-1} of RGDV (pharmacophore control of DTCC–RGDV, $P < 0.05$). $n = 12$.

(3*S*)-1-[(5,5-dimethyl-3,4-dioxan-1-yl)-1,2,3,4-tetrahydro-β-carbolin-3-carboxylate (**2**), **3** (DTCC), (3*S*)-1-[(5,5-dimethyl-3,4-dioxan-1-yl)-1,2,3,4-tetrahydro-β-carbolin-3-carboxyl-Arg(NO_2)-Gly-Asp(OBzl)-Val-OBzl (**4**) and (3*S*)-1-[(5,5-dimethyl-3,4-dioxan-1-yl)-1,2,3,4-tetrahydro-β-carbo-lin-3-carboxyl-Arg-Gly-Asp-Val (**5**, DTCC–RGDV). The yields of **1**, **2**, **3**, **4**, and **5** were 81%, 37%, 91%, 90% and 92%, respectively. The HPLC purity of DTCC–RGDV was 97.6%. These mean that DTCC–RGDV can be satisfactorily prepared by using the present synthetic route.

FT-ICR-MS spectra showing DTCC–RGDV existing as a trimer

The trimer of DTCC–RGDV was explored by the FT-ICR-MS spectra. Fig. 3A shows the full spectrum of DTCC–RGDV. The full spectrum gave an ion peak of the monomer plus H at 744.36409 (theoretical value, 744.36806), an ion peak of the dimer plus H at 1487.72714 (theoretical value, 1487.72830), and a divalent ion peak of the trimer plus H at 1116.04720 (theoretical value, 1116.04819). These ion peaks suggested that in the measuring condition of

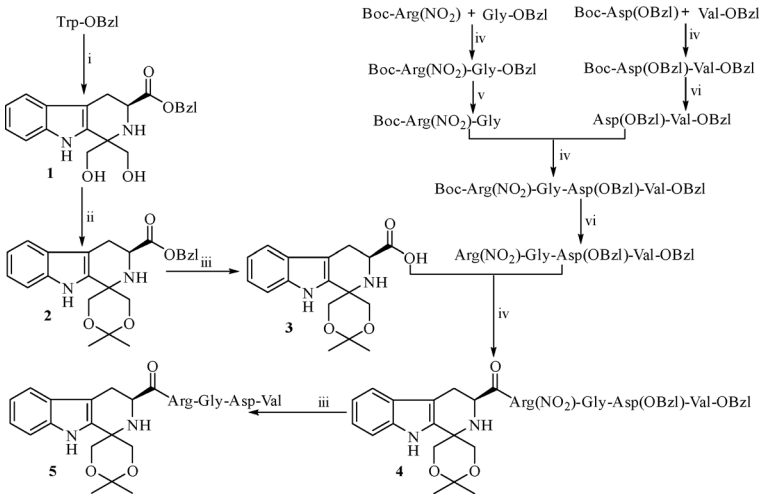

Scheme 1 Synthetic route to DTCC–RGDV (**5**); (i) CF_3CO_2H and 1,3-dihydroxyacetone; (ii) H_2SO_4 and $MgSO_4$; (iii) H_2 and Pd/C; (iv) HOBt and DCC; (v) NaOH and HCl; and (vi) ethyl acetate solution of hydrogen chloride (4N).

ESI-FT-ICR-MS, a timer of DTCC–RGDV formed a monomer and a dimer.

To confirm that the monomer and the dimer were the fragments of the trimer, the qCID spectrum was measured. Fig. 3B is the qCID spectrum of the ion peak of 1116.04720. The qCID spectrum gave an ion peak of the monomer plus H at 744.36409 (theoretical value, 744.36806) and an ion peak of the dimer plus H at 1487.72714 (theoretical value, 1487.72830). These ion peaks suggested that the monomer and the dimer were the fragments of the trimer of DTCC–RGDV. Therefore, the trimer is the sole existing form of DTCC–RGDV indeed.

The manner of DTCC–RGDV forming the trimer

Considering the three cross-peaks reflecting the intermolecular association pattern of three molecules, the NOESY 2D NMR spectrum of DTCC–RGDV was measured. Fig. 4 shows that there were three interesting cross-peaks marked with red circles. Of the three cross-peaks, cross-peak 1 resulted from the interaction of the pyrrole H and the carboline 4-H, cross-peak 2 resulted from the interaction of the pyrrole H and the carboline 7-H, and cross-peak 3 resulted from the interaction of the carboline 7-H and the methyl H of the 1,3-dioxane of the carboline. These cross-peaks explore a spatial relationship for three molecules of DTCC–RGDV. According to the spatial relationship, the distance between the mentioned H atoms should be less than 4 Å. To build the trimer, the energy minimization was performed to give energy a minimized conformation for DTCC–RGDV. Based on the distances of the mentioned H atoms and using the energy-minimized conformation, three molecules of DTCC–RGDV were manually accessed, which led the trimer of DTCC–RGDV to a three-leaf electric fan-like conformation.

Tyndall effect of DTCC–RGDV in ultrapure water

The nano-property was shown by the Tyndall effect of the solution of DTCC–RGDV in ultrapure water. The Tyndall effect could be generally used to characterize the particles in the colloid, the suspension and the nano-solution, a transparent solution. For colloid and suspension, the size of the particles is more than 1000 nanometers in diameter, while for the nano-solution, the size of the particles is less than 150 nanometers in diameter. Fig. 5A and B show that with and without laser irradiation, ultrapure water exhibits no Tyndall effect. Fig. 5C, E, and G show that without laser irradiation, the aqueous solution of DTCC–RGDV in ultrapure water (final concentration, 1 μM, 0.1 μM, and 0.01 μM) exhibited no Tyndall effect. Fig. 5D, F, and H show that with laser irradiation, the aqueous solution of DTCC–RGDV in ultrapure water exhibited the Tyndall effect. Therefore, the Tyndall effect explored that the aqueous solution of DTCC–RGDV in ultrapure water was a nano-solution.

Stability of the nano-solution of DTCC–RGDV in ultrapure water

To show the stability of the nano-property, the particle size and zeta potential of the aqueous solution of DTCC–RGDV in ultrapure water (final concentration, 1 μM) were tested for successive 7 days. Fig. 6 shows that within 7 days, the size of the nanoparticles was 135 nm–185 nm in diameter, and the zeta potential on the surface of the nano-particle was −40.3 mV to −49.7 mV. These data meant that in 7 days, the nano-property of the aqueous solution of DTCC–RGDV in ultrapure water was stable enough.

TEM image and the nanoparticles of DTCC–RGDV

To show the nano-feature of DTCC–RGDV in ultrapure water, the TEM images were tested. Fig. 7A shows that in ultrapure water (final concentration, 1 μM), DTCC–RGDV formed nanoparticles of 27 nm–130 nm diameter. Fig. 7B shows that in ultrapure water (final concentration, 0.1 μM), DTCC–RGDV formed nanoparticles of 31 nm–125 nm diameter. Fig. 7C shows that in ultrapure water (final concentration, 0.01 μM),

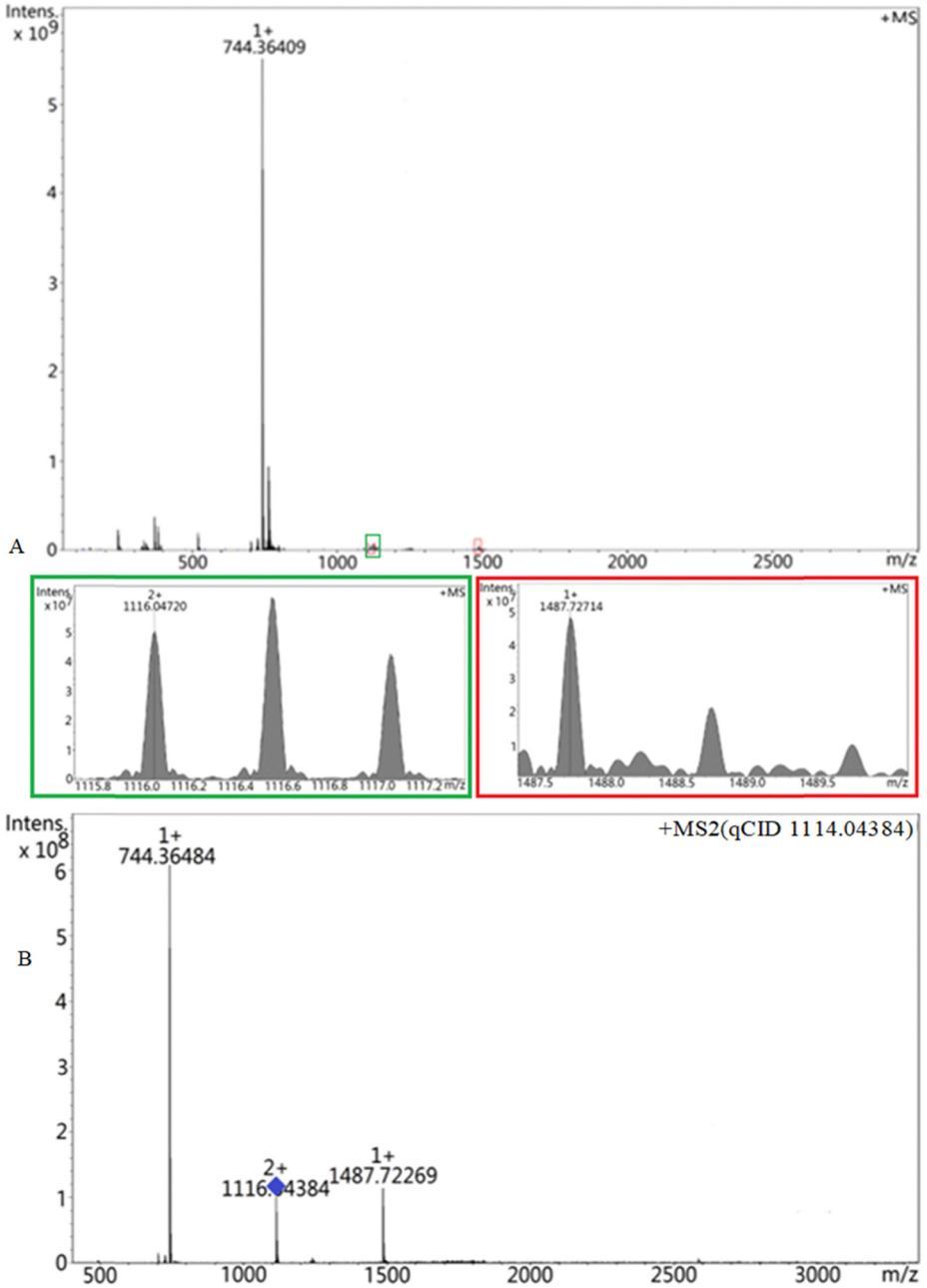

Fig. 3 ESI-FT-ICR-MS full spectrum and qCID spectrum of DTCC–RGDV. (A) Full spectrum of DTCC–RGDV giving an ion peak of the monomer plus H at 744.36409 (theoretical value, 744.36806), an ion peak of the dimer plus H at 1487.72714 (theoretical value, 1487.72830), and a divalent ion peak of the trimer plus H at 1116.04720 (theoretical value, 1116.04819). (B) qCID spectrum of the trimer of DTCC–RGDV: the collision-induced dissociation of the ion peak at 1116.04720, *i.e.* the trimer, giving an ion peak at 744.36484 (mass of monomer plus H) and an ion peak at 1487.72269 (mass of dimer plus H); both are locally magnified here.

DTCC–RGDV formed nanoparticles of 35 nm–109 nm diameter. Therefore, the concentration did not significantly change the shape and the size of the particles.

SEM image and the lyophilized powders of DTCC–RGDV

To show the nano-feature of the lyophilized powders prepared from the aqueous solution of DTCC–RGDV in ultrapure water, the SEM images were analyzed. Fig. 8A shows that the lyophilized powders prepared from the aqueous solution of DTCC–RGDV in ultrapure water (1 μM) were nanoparticles of 70 nm–170 nm diameter. Fig. 8B shows that the lyophilized powders prepared from the aqueous solution of DTCC–RGDV in ultrapure water (0.1 μM) were nanoparticles of 97 nm–190 nm diameter. Fig. 8C shows that the lyophilized powders prepared from the aqueous solution of DTCC–RGDV in ultrapure water (0.01 μM) were nanoparticles of 87 nm–163 nm diameter. Therefore, the concentration did not significantly change the shape and the size of the lyophilized powders.

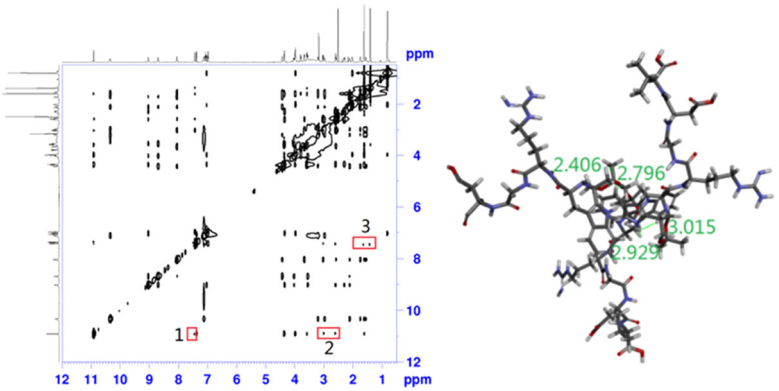

Fig. 4 H–H NOESY 2DNMR spectrum of DTCC–RGDV: three interesting cross-peaks were marked by red circles, cross-peak 1 from the interaction of the pyrrole H and the carboline 4-H, cross-peak 2 from the interaction of the pyrrole H and the carboline 7-H, cross-peak 3 from the interaction of the carboline 7-H and the methyl H of 1,3-dioxane of the carboline. These cross-peaks explored the spatial distance between the three molecules of DTCC–RGDV. The distance between the mentioned H should be less than 4 Å; accordingly, three energy-minimized molecules of DTCC–RGDV were manually accessed to form the trimer and gave a three-leaf electric fan-like conformation.

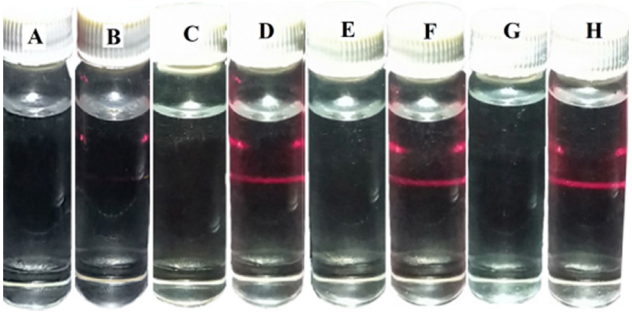

Fig. 5 Tyndall effect of the solution of DTCC–RGDV in ultrapure water: (A) ultrapure water without laser irradiation; (B) ultrapure water with laser irradiation; (C) aqueous solution of DTCC–RGDV in ultrapure water (1 μM) without laser irradiation; (D) aqueous solution of DTCC–RGDV in ultrapure water (1 μM) with laser irradiation; (E) aqueous solution of DTCC–RGDV in ultrapure water (0.1 μM) without laser irradiation; (F) aqueous solution of DTCC–RGDV in ultrapure water (0.1 μM) with laser irradiation; (G) aqueous solution of DTCC–RGDV in ultrapure water (0.01 μM) without laser irradiation; and (H) aqueous solution of DTCC–RGDV in ultrapure water (0.01 μM) with laser irradiation.

AFM image and the nanoparticles of DTCC–RGDV in rat plasma

To show the nano-feature of DTCC–RGDV in rat plasma, the AFM image was analyzed. Fig. 9A shows that rat plasma itself had no nano-particle. Fig. 9B shows that in rat plasma (1 μM), DTCC–RGDV formed nanoparticles of 52 nm–73 nm height. Fig. 9C shows that in rat plasma (0.1 μM), DTCC–RGDV formed nanoparticles of 47 nm–65 nm height. Fig. 9D shows that in rat plasma (0.01 μM), DTCC–RGDV formed nanoparticles of 44 nm–75 nm height. Therefore, the concentration did not significantly change the shape and height of the particles.

In vitro action of DTCC–RGDV on platelets, erythrocytes and leucocytes

To examine the *in vitro* capacity of DTCC–RGDV binding platelets, erythrocytes and leucocytes, the AFM images were measured. According to the general procedure, the platelets, erythrocytes, and leucocytes of rats were collected, and a solution of DTCC–RGDV in ultrapure water of pH 6.7 (1 μM) was used to treat the platelets, the erythrocytes, and the leucocytes for measuring the AFM image. Fig. 10A shows that the resting platelets without DTCC–RGDV had a smooth surface. Fig. 10B shows that the resting platelets with DTCC–RGDV had unsmooth surface. Fig. 10C shows that erythrocytes without DTCC–RGDV had a smooth surface. Fig. 10D shows that erythrocytes with DTCC–RGDV also had a smooth surface. Fig. 10E shows that leucocytes without DTCC–RGDV had smooth surface. Fig. 10F shows that leucocytes with DTCC–RGDV also had smooth surface. These images suggested that DTCC–RGDV was only capable of binding onto the surface of the resting platelets.

In vitro action of DTCC–RGDV on AA-activated platelets

To examine the *in vitro* capacity of DTCC–RGDV in preventing platelets from the aggregation induced by arachidonic acid (AA, 7.5 mg mL^{-1}), the platelets were pre-incubated with NS or DTCC–RGDV, and then activated with AA. Fig. 11A shows the AFM image after 15-minute incubation of NS, which showed that no pseudopodia occurred on the surface of the platelets. Fig. 11B shows the AFM image after 15-minute incubation of 1 μM DTCC–RGDV, which showed that AA activation did not induce aggregation. Fig. 11C shows the AFM image after 15-minute incubation of 0.1 μM DTCC–RGDV, which showed that, compared to 15-minute incubation of 1 μM DTCC–RGDV, AA activation induced more aggregation. Fig. 11D shows the AFM image after 15-minute incubation of 0.01 μM DTCC–RGDV, which showed that, compared to the 15-minute incubation of 0.1 μM DTCC–RGDV, AA activation induced more aggregation. Fig. 11E shows the AFM image after 15-minute incubation of NS, which showed that, compared to 15-minute incubation of 0.01 μM DTCC–RGDV, AA activation induced a large number of platelets to aggregate. Collectively, the AFM images demonstrate

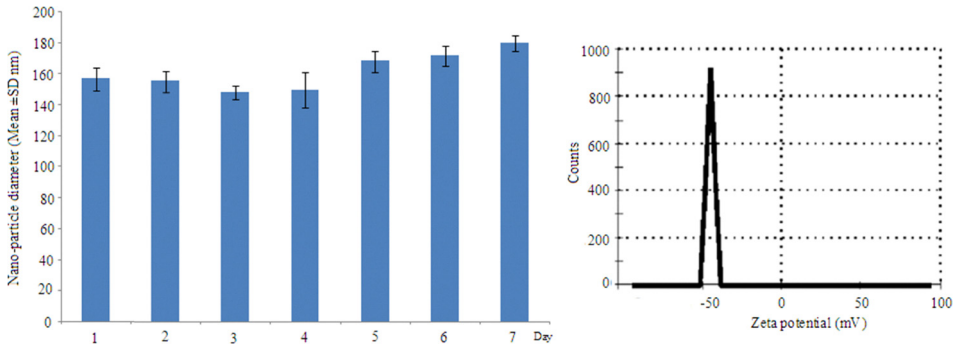

Fig. 6 In 7 days, the particle size and the zeta potential of an aqueous solution of DPC–RGDV in ultrapure water (1 μM): the size of the nanoparticles ranged from 135 nm to 185 nm in diameter, while the zeta potential ranged from −40.3 mV to −49.7 mV.

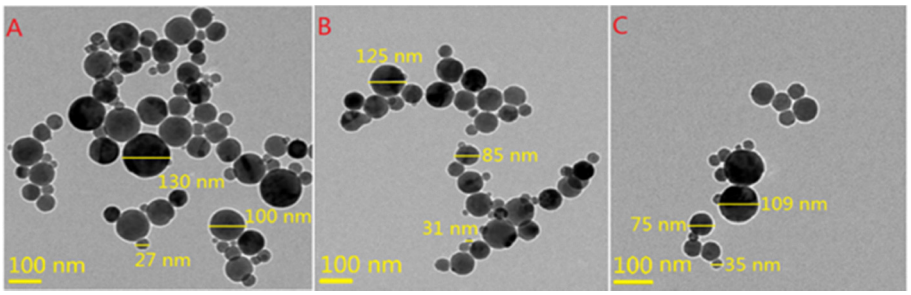

Fig. 7 TEM images of DTCC–RGDV in ultrapure water: (A) in aqueous solution (1 μM), DTCC–RGDV formed nanoparticles with diameters of 27 nm–130 nm. (B) In aqueous solution (0.1 μM), DTCC–RGDV formed nanoparticles with diameters of 31 nm–125 nm. (C) In aqueous solution (0.01 μM), DTCC–RGDV formed nanoparticles with diameters of 35 nm–105 nm.

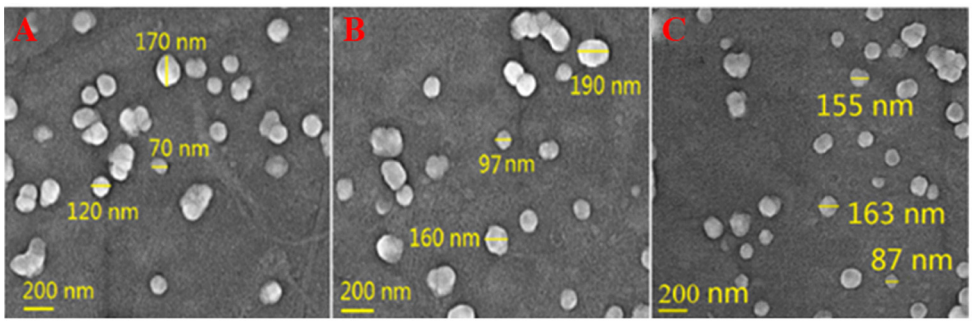

Fig. 8 SEM images of the lyophilized powders of DTCC–RGDV: (A) SEM image of the lyophilized powders prepared from the aqueous solution of DTCC–RGDV in ultrapure water (1 μM). (B) SEM image of the lyophilized powders prepared from the aqueous solution of DTCC–RGDV in ultrapure water (0.1 μM). (C) SEM image of the lyophilized powders prepared from the aqueous solution of DTCC–RGDV in ultrapure water (0.01 μM).

that DTCC–RGDV can prevent platelet activation and aggregation in a concentration-dependent manner.

In vivo DTCC–RGDV inhibiting arterial thrombosis

The *in vivo* activity of DTCC–RGDV inhibiting arterial thrombosis was evaluated in a rat thread model, and the thrombus weight was used to represent the activity. In this assay, NS (3 mL kg^{-1}, negative control), the suspension of aspirin in NS (167 μmol kg^{-1}, positive control), the suspension of DTCC in NS (1 μmol kg^{-1}, pharmacophore control), and the suspension of DTCC–RGDV in NS (0.01 μmol kg^{-1}) were orally given to male Sprague-Dawley rats (230–270 g, each 12 rats).

Fig. 12A shows that the arterial thrombus weight of the rats orally treated with 0.01 μmol kg^{-1} of DTCC–RGDV was significantly lower than that of the rats orally treated with NS ($p < 0.01$), while the arterial thrombus weight of the rats orally treated with 0.01 μmol kg^{-1} of DTCC–RGDV was equal to those of the rats orally treated with 1 μmol kg^{-1} of DTCC and 167 μmol kg^{-1} of aspirin ($p > 0.05$). Thus, the activity of

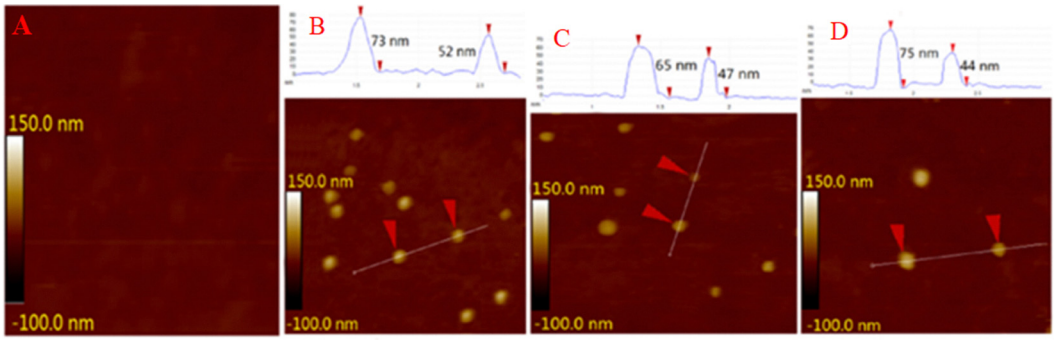

Fig. 9 AFM images of DTCC–RGDV in the rat plasma: (A) rat plasma itself had no comparable particles. (B) In rat plasma (1 μM), DTCC–RGDV formed nanoparticles with heights of 52 nm–73 nm. (C) In rat plasma (0.1 μM), DTCC–RGDV formed nanoparticles with heights of 47 nm–65 nm. (D) In rat plasma (0.01 μM), DTCC–RGDV formed nanoparticles with heights of 44 nm–75 nm.

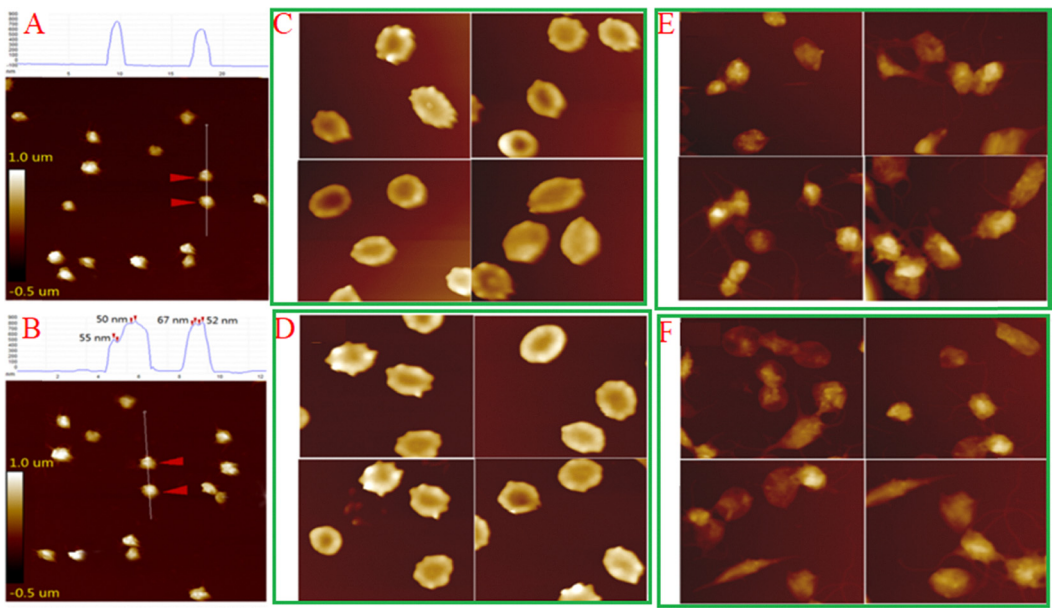

Fig. 10 *In vitro* action of DTCC–RGDV on platelets, erythrocytes and leucocytes: (A) resting platelets without DTCC–RGDV (1 μM) having a smooth surface. (B) Resting platelets with DTCC–RGDV (1 μM) having an unsmooth surface. (C) Erythrocytes without DTCC–RGDV (1 μM) having smooth surface. (D) Erythrocytes with DTCC–RGDV (1 μM) having a smooth surface. (E) Leucocytes without DTCC–RGDV (1 μM) having a smooth surface. (F) Leucocytes with DTCC–RGDV (1 μM) having a smooth surface.

DTCC–RGDV inhibiting arterial thrombosis was 100 times and 16 700 times that of DTCC and aspirin, respectively.

Fig. 12B shows that the concentration of P-selectin in the plasma of 0.01 μmol kg^{-1} of DTCC–RGDV-treated rats in the arterial thrombosis condition was significantly less than that of NS and 1 μmol kg^{-1} of DTCC-treated rats in the arterial thrombosis condition ($p < 0.01$).

Fig. 12C shows that the concentration of GPIIb/IIIa in the plasma of 0.01 μmol kg^{-1} of DTCC–RGDV-treated rats in the arterial thrombosis condition was significantly less than that of NS and 1 μmol kg^{-1} of DTCC-treated rats in the arterial thrombosis condition ($p < 0.01$).

Fig. 12A–C together show that DTCC–RGDV was an excellent anti-arterial thrombus agent.

DTCC–RGDV targets arterial thrombus with subsequent release of DTCC

To examine the action of DTCC–RGDV in arterial thrombus, the homogenate extracts of the arterial thrombus, blood, heart, liver, spleen, kidney, and brain of the rats treated with NS and 0.1 μmol kg^{-1} of DTCC–RGDV were prepared for FT-ICR-MS analysis by using a liquid–liquid extraction. The thrombus, blood, heart, liver, spleen, kidney, and brain of the rats were homogenized after dilution in ultrapure water and then extracted with ethyl acetate. The samples received ultrasonic extraction for 30 minutes and centrifugal separation for 15 minutes (4000 g). The upper layer was separated and evaporated over N_2 gas at 37 °C. The residue was dissolved in

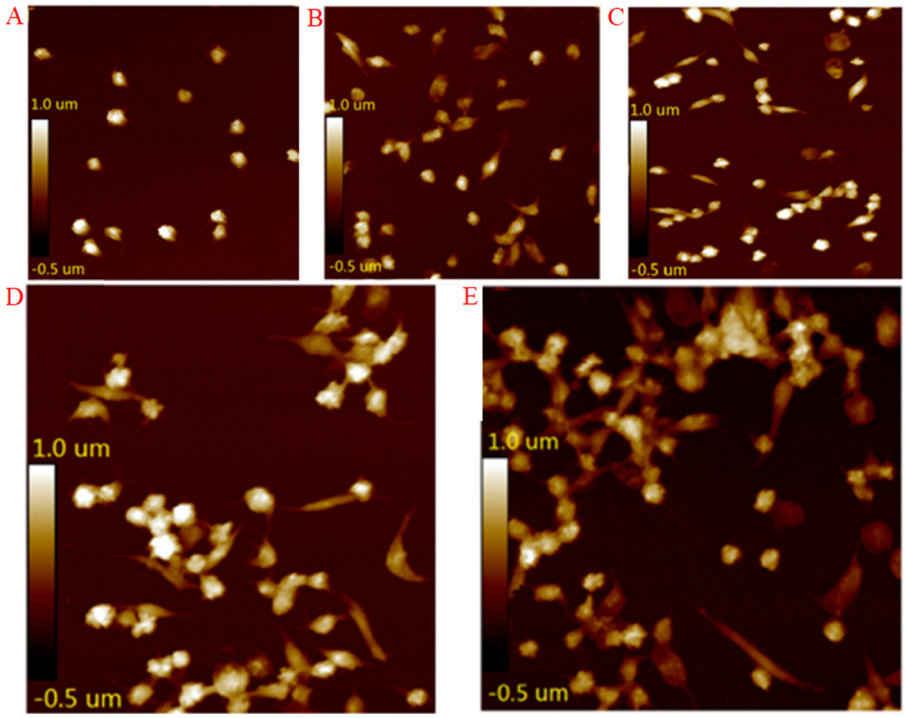

Fig. 11 AFM imaged *in vitro* effect of DTCC–RGDV on AA activated platelets: (A) after 15-minnute incubation of NS, the AFM image shows platelets having smooth surface and no pseudopodia on the platelet surface. (B) After 15-minute incubation of DTCC–RGDV (1 μM) and then activation by AA (7.5 mg mL^{-1}), the AFM image shows pseudopodia occurring on the surface of a few platelets. (C) After 15-minute incubation of DTCC–RGDV (0.1 μM) and then activation by AA (7.5 mg mL^{-1}), the AFM image shows more platelets in a state of aggregation. (D) After 15-minute incubation of DTCC–RGDV (0.01 μM) and then activation by AA (7.5 mg mL^{-1}), the AFM image shows a large number of platelets in a state of aggregation. (E) After 15-minute incubation of NS and then activation by AA (7.5 mg mL^{-1}), the AFM image shows almost all platelets in a state of aggregation.

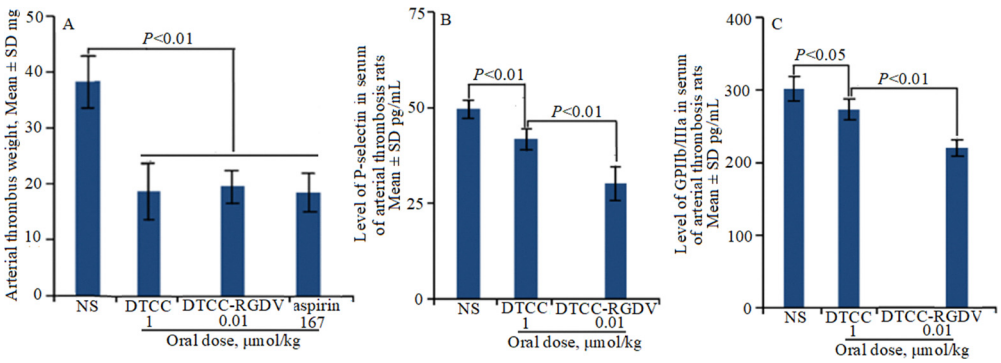

Fig. 12 *In vivo* effects of DTCC–RGDV on arterial thrombus weight and on plasma concentrations of P-selectin and GPIIb/IIIa. (A) At 0.01 μmol kg^{-1} of oral dose DTCC–RGDV significantly reducing the rats to form arterial thrombus, the arterial thrombus weight been equal to those of the rats orally treated by 1 μmol kg^{-1} of DTCC and 167 μmol kg^{-1} of aspirin; (B) The concentration of P-selectin in the plasma of 0.01 μmol kg^{-1} of DTCC–RGDV treated rats in arterial thrombosis condition been significantly less than those of NS and 1 μmol kg^{-1} of DTCC treated rats in arterial thrombosis condition; (C) The concentration of GPIIb/IIIa in the plasma of 0.01 μmol kg^{-1} of DTCC–RGDV treated rats with arterial thrombosis been significantly less than those of NS and 1 μmol kg^{-1} of DTCC treated rats in arterial thrombosis condition; n = 12.

chromatographically pure methanol (200 μL methanol per gram of tissue) for analysis.

Fig. 13A shows the locally amplified spectra displaying a peak of Arg-Gly plus H at 232.14340 (theoretical value: 232.14096), a peak of Asp-Val plus H at 233.11397 (theoretical value: 233.11375), a peak of Arg-Gly-Asp-Val plus H at 446.23779 (theoretical value: 446.23632), a peak of DTCC plus H at 317.14760 (theoretical value: 317.15013) and a peak of DTCC–RGDV plus H at 744.36630 (theoretical value: 744.36806). It was also found that the locally amplified spectra of the homogenate extracts of the arterial thrombus, blood, heart, liver, spleen, kidney, and brain of the rats treated with NS showed no comparable peaks. Similarly, the locally amplified spectra of the homogenate extracts of the blood, heart, liver, spleen,

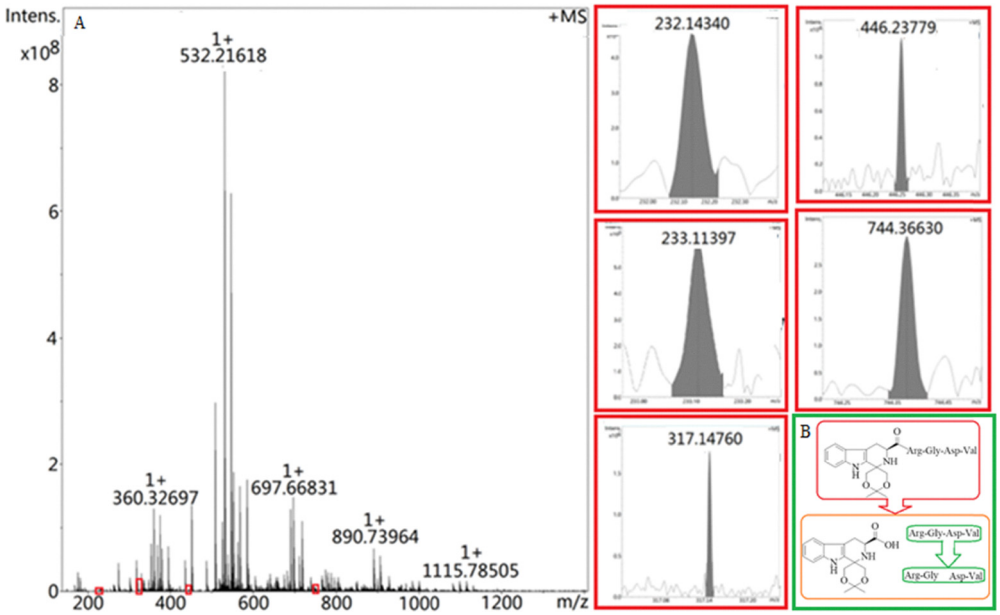

Fig. 13 FT-ICR-MS test of the homogenate extracts of the arterial thrombus of the rat orally treated by 0.1 μmol kg^{-1} of DTCC–RGDV. (A) FT-ICR-MS spectra. The locally amplified spectra giving the peak of Arg-Gly plus H at 232.14340 (theoretical value: 232.14096), the peak of Asp-Val plus H at 233.11397 (theoretical value: 233.11375), the peak of Arg-Gly-Asp-Val plus H at 446.23779 (theoretical value: 446.23632), the peak of DTCC plus H at 317.14760 (theoretical value: 317.15013) and the peak of DTCC–RGDV plus H at 744.36630 (theoretical value: 744.36806); While the locally amplified spectra of the homogenate extracts of the arterial thrombus, blood, heart, liver, spleen, kidney and brain of the rats treated by NS giving no the same peaks; Similarly, the locally amplified spectra of the homogenate extracts of the blood, heart, liver, spleen, kidney and brain of the rats treated by 0.1 μmol kg^{-1} of DTCC–RGDV giving no comparable peaks; (B) The process of DTCC–RGDV releasing DTCC in arterial thrombus.

kidney, and brain of the rats treated with 0.1 μmol kg^{-1} of DTCC–RGDV gave no comparable peaks. Thus, the FT-ICR-MS spectra of the homogenate extracts of the rats confirmed DTCC–RGDV as an arterial thrombus targeting agent.

Based on the results of Fig. 13A, the release of DTCC from DTCC–RGDV in the arterial thrombus could be described with Fig. 13B. In arterial thrombus, DTCC–RGDV was first divided into DTCC and Arg-Gly-Asp-Val, then Arg-Gly-Asp-Val was divided into Arg-Gly and Asp-Val.

As shown in Fig. 2B, the oral dose of RGDV was 20 times higher than that of DTCC, and in terms of the anti-arterial thrombosis effect of DTCC, the anti-arterial thrombotic action of RGDV was negligible.

Considering both the release of DTCC from DTCC–RGDVF shown in Fig. 13B and the importance of DTCC in inhibiting arterial thrombosis as demonstrated by the analysis in Fig. 2B, it can be concluded that DTCC–RGDV targets arterial thrombus and releases DTCC. This mechanism is responsible for the excellent anti-arterial thrombotic action of the nano-scaled DTCC–RGDV.

Table 2 Effect of DTCC–RGDV on serum Cr and BUN

Group	Cr, mean ± SD (μM)	BUN, mean ± SD (mM)
NS	20.8 ± 3.2	14.6 ± 2.0
DTCC–RGDV	21.1 ± 3.0[a]	14.1 ± 1.6[a]

[a] Compare with NS, $p > 0.05$, and $n = 12$.

DTCC–RGDV does not injure the kidney

To estimate the safety, the toxicity of DTCC–RGDV to kidney was addressed by the serum creatinine (Cr) and blood urea nitrogen (BUN) of the rats in the *in vivo* arterial thrombus weight assay, *i.e.* the serum Cr and BUN of the arterial thrombosis rats treated with NS or 0.1 μmol kg^{-1} of DTCC–RGDV. The serum Cr and BUN were measured by following the procedures provided with the corresponding kits (serum Cr: Nanjing Jiancheng Bioengineering Institute, PR China; BUN: Shanghai Lianshuo Biological Technology Co., Ltd, PR China). Table 2 shows that the serum Cr and BUN of the rats treated with DTCC–RGDV are equal to those of the rats treated with NS. Therefore, DTCC–RGDV does not injure the kidney of the rats.

DTCC–RGDV does not injure the liver

To estimate the safety, the toxicity of DTCC–RGDV in the liver was addressed by the serum alanine aminotransferase (ALT/GPT) and serum aspartic aminotransferase (AST/GOT) of the rats in the *in vivo* arterial thrombus weight assay, *i.e.* the serum

Table 3 Effect of DTCC–RGDV on serum ALT/GPT and AST/GOT

Group	ALT/GPT, mean ± SD Carmen's unit	AST/GOT, mean ± SD Carmen's unit
NS	54.7 ± 4.2	100.43 ± 8.6
DTCC–RGDV	55.3 ± 4.3[a]	100.49 ± 8.4[a]

[a] Compare with NS, $p > 0.05$, and $n = 12$.

ALT/GPT and AST/GOT of the arterial thrombosis rats treated with NS or 0.1 μmol kg^{-1} of DTCC–RGDV. The serum ALT/GPT was measured by following the procedure of the kit provided by Nanjing Jiancheng Bioengineering Institute, PR China, while the serum AST/GOT was measured by following the procedure of the kit provided by Nanjing Jiancheng Bioengineering Institute, PR China. Table 3 shows that the serum ALT/GPT and AST/GOT of the rats treated with DTCC–RGDV are equal to those of the rats treated with NS. Therefore, DTCC–RGDV does not injure the liver of the rats.

Conclusions

Coupling the anti-arterial thrombus-active DTCC and RGDV, thereby preparing DTCC–RGDV, is a successful strategy. This paper explored that in water, DTCC–RGDV existed as a trimer, thereby forming nanoparticles with a suitable diameter for safe transport *via* blood circulation. By binding to platelets, DTCC–RGDV nanoparticles enter the active pockets of P-selectin and GPIIb/IIIa on the platelet surface, leading to decreased plasma levels of these biomarkers. This process enables targeted delivery of DTCC–RGDV to arterial thrombi and release of the anti-thrombotic agent DTCC, establishing P-selectin and GPIIb/IIIa as the key molecular mechanisms underlying its anti-arterial thrombotic activity. The target action of DTCC–RGDV ensured that it did not injure the kidneys or livers of the treated rats. Therefore, nano-scaled DTCC–RGDV is an excellent candidate for the development of nano-medicines for inhibiting arterial thrombosis.

Author contributions

Xiaoyi Zhang: conceptualization, formal analysis, investigation, writing – editing. Yifan Yang: data curation, formal analysis, investigation, writing – review. Dongxu Wu: data curation, investigation, writing – review & editing. Yaonan Wang and Shurui Zhao: data curation. Jianhui Wu: formal analysis. Ming Zhao: conceptualization, formal analysis, funding acquisition, project administration. Shiqi Peng: conceptualization, project administration, supervision, writing – original draft, review & editing.

Conflicts of interest

There are no conflicts to declare.

Abbreviations

DTCC	(3*S*)-1-[(5,5-Dimethyl-3,4-dioxan-1-yl)-1,2,3,4-tetrahydro-β-carboline-3-carboxylic acid
STCCs	(3*S*)-1-Substituted-1,2,3,4-tetrahydro-β-carboline-3-carboclic acids
THF	Anhydrous tetrahydrofuran
HOBt	1-Hydroxybenzotriazole
DCC	Dicyclohexylcarbodiimide
NMM	*N*-Methylmorpholine

Data availability

Supplementary information is available. See DOI: https://doi.org/10.1039/d6ma00386a.

The authors confirm that the data supporting the findings of this study are available within the article.

Acknowledgements

The authors of this paper extend their appreciation to the Engineering Research Center of Endogenous Prophylactic of the Ministry of Education of China and NSFC (81703332) for the financial support.

Notes and references

1 E. Tóth, *et al.*, Fibrin to von Willebrand factor ratio in arterial thrombi is associated with plasma levels of inflammatory biomarkers and local abundance of extracellular DNA, *Thromb. Res.*, 2022, **209**, 8–15.
2 B. B. Shi, *et al.*, Accelerating thrombolysis of arterial thrombus with NO-MBs UTMD therapy, *Eur. J. Pharm. Biopharm.*, 2024, **205**, 114566.
3 Y. M. Puspitasari, *et al.*, Hutchinson-Gilford progeria syndrome mice display accelerated arterial thrombus formation and increased platelet reactivity, *Thromb. Res.*, 2024, **241**, 109100.
4 J. R. Munaim, *et al.*, Simulaneous arterial and venous system thrombus in patient with suspected malignancy, *J. Am. Coll. Cardiol.*, 2024, **83**(13), 4168.
5 M. D. P. B. Molano, *et al.*, Life-Threatening Hemoptysis and Bradycardia in Metastatic Sarcoma with Vascular Invasion and Left Atrial Tumor Thrombus: The Role of Arterial Embolization, *J. Vasc. Interventional Radiol.*, 2025, **36**(3), 537–539.
6 N. J. Jooss, *et al.*, Platelet glycoprotein VI cluster size is related to thrombus formation and phosphatidylserine exposure in collagen-adherent platelets under arterial shear, *J. Thromb. Haemostasis*, 2023, **21**(8), 2260–2267.
7 M. A. Zeligs, *et al.*, 3,3′-Diindolylmethane reduces fibrin content, neutrophils, and neutrophil extracellular traps (NETs) in carotid arterial thrombi-Relevance for improved acute ischemic stroke (AIS) thrombectomy, *Neurotherapeutics*, 2025, **22**(4), e00643.
8 C. G. Suen, *et al.*, Intracranial high-resolution vessel wall imaging in differentiating intraluminal basilar artery thrombus from arterial dissection, Interdisciplinary, *Neurosurgery*, 2020, **22**, 100841.
9 A. C. Kidd, *et al.*, Acute arterial occlusion due to abdominal aortic tumour-thrombus in relapsed osteosarcoma: A case report, *The Royal College of Radiologists Open*, 2025, vol. 3, p. 100344.
10 C. Sugita, *et al.*, Elevated plasma levels of factor VIII enhance arterial thrombus formation on erosive smooth muscle cell-rich neointima but not normal intima in rabbits, *Thromb. Res.*, 2024, **238**, 185–196.

11 Y. M. Puspitasari, *et al.*, Hutchinson-Gilford progeria syndrome mice display accelerated arterial thrombus formation and increased platelet reactivity, *Thromb. Res.*, 2024, **241**, 109100.
12 C. Gianni, *et al.*, Percutaneous Aspiration Thrombectomy in Patients With Persistent Left Atrial Appendage Thrombus: A Case Series, *Clin. Electrophysiol.*, 2025, **11**(11), 2448–2457.
13 J. Weisel, *et al.*, Exploring the thrombus niche: Lessons learned and potential therapeutic opportunities, *Blood*, 2025, **146**(12), 1389–1399.
14 B. O. Al-Najjar, *et al.*, P2Y12 antagonists: Approved drugs, potential naturally isolated and synthesised compounds, and related in-silico studies, *Eur. J. Med. Chem.*, 2022, **227**, 113924.
15 X. Zhang, *et al.*, Optimization of physicochemical properties of pyridone-based EP3 receptor antagonists, *Bioorg. Med. Chem. Lett.*, 2021, **47**, 128172.
16 C. L. Jayne, *et al.*, Discovery of hydroxy pyrimidine Factor IXa inhibitors, *Bioorg. Med. Chem. Lett.*, 2020, **30**, 127279.
17 D. Babkov, *et al.*, 3-Arylidene-2-oxindoles as GSK3βinhibitors and anti-thrombotic agents, *Bioorg. Med. Chem. Lett.*, 2023, **87**, 129283.
18 S. Liu, *et al.*, Protease activated receptor 4 (PAR4) antagonists: Research progress on small molecules in the field of antiplatelet agents, *Eur. J. Med. Chem.*, 2021, **209**, 112893.
19 N. Qin, *et al.*, Recent research progress of Uncaria spp. based on alkaloids: phytochemistry, pharmacology and structural chemistry, *Eur. J. Med. Chem.*, 2021, **210**, 112960.
20 J. H. Bourne, *et al.*, Hydroxychloroquine inhibits hemolysis-induced arterial thrombosis ex vivo and improves lung perfusion in hemin-treated mice, *J. Thromb. Haemostasis*, 2024, **22**, 2018–2026.
21 Z. Li, *et al.*, Heptapeptide -based modification leading to enhancing the action of MTCA on activated platelets, P-selectin, GPIIb/IIIa, *Future Med. Chem.*, 2018, **10**(16), 1957–1970.
22 X. X. Yuan, *et al.*, RGDS-modified ursolic acid: insights into self-assembly, nano-properties, osteoporosis inhibition and molecular mechanisms, *J. Mater. Chem. B*, 2025, **13**(20), 5776–5788.
23 Y. Y. Li, *et al.*, PTX-RPPR, a conjugate of paclitaxel and NRP-1 peptide inhibitor to prevent tumor growth and metastasis, *Biomed. Pharmacother.*, 2024, **178**, 117264.